NANO LETTERS

pubs.acs.org/NanoLett Letter

Self-Assembled 3D Nanosplit Rings for Plasmon-Enhanced Optofluidic Sensing

Chunhui Dai, Zihao Lin, Kriti Agarwal, Carol Mikhael, Anupam Aich, Kalpna Gupta, and Jeong-Hyun Cho*

Cite This: *Nano Lett.* 2020, 20, 6697−6705 Read Online

ACCESS | Metrics & More | Article Recommendations | Supporting Information

ABSTRACT: Plasmonic sensors are commonly defined on two-dimensional (2D) surfaces with an enhanced electromagnetic field only near the surface, which requires precise positioning of the targeted molecules within hotspots. To address this challenge, we realize segmented nanocylinders that incorporate plasmonic (1−50 nm) gaps within three-dimensional (3D) nanostructures (nanocylinders) using electron irradiation triggered self-assembly. The 3D structures allow desired plasmonic patterns on their inner cylindrical walls forming the nanofluidic channels. The nanocylinders bridge nanoplasmonics and nanofluidics by achieving electromagnetic field enhancement and fluid confinement simultaneously. This hybrid system enables rapid diffusion of targeted species to the larger spatial hotspots in the 3D plasmonic structures, leading to enhanced interactions that contribute to a higher sensitivity. This concept has been demonstrated by characterizing an optical response of the 3D plasmonic nanostructures using surface-enhanced Raman spectroscopy (SERS), which shows enhancement over a 22 times higher intensity for hemoglobin fingerprints with nanocylinders compared to 2D nanostructures.

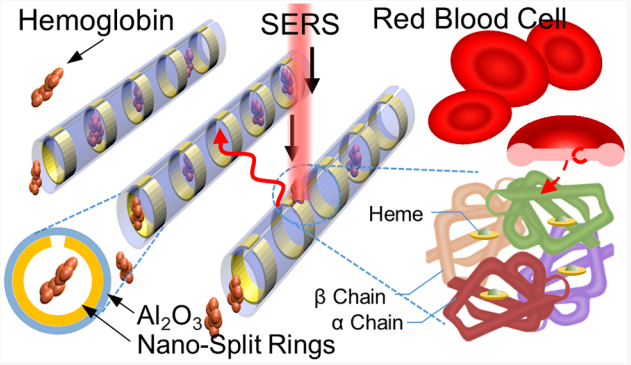

KEYWORDS: *self-assembly, nanofluidics, plasmonics, Raman, 3D, nanosplit rings*

Plasmonic sensing has arisen to be a powerful technique for detecting and identifying chemical and biological components.[1−10] Nanostructured metallic surfaces confine electromagnetic (EM) waves and form localized surface plasmon (LSP), leading to strong localized field enhancement,[11] which benefits plasmonic sensing techniques such as surface-enhanced Raman Scattering (SERS)[3,4,6,9,12,13] and surface-enhanced infrared absorption (SEIRA).[5,7,10,14−16] As the sensing signal transduced strongly depends on the size and shape of the nanostructures,[3] tremendous efforts have been put into the innovation of advanced fabrication techniques for achieving well-defined nanoscale plasmonic structures, including electron beam lithography,[10,11,17−19] nanosphere lithography,[6,13,20,21] template stripping,[2,12,15,22] electrochemical growth,[3] and DNA self-assembly.[23,24] However, most of these structures are demonstrated on planar 2D surfaces with an enhanced EM field only near the surface,[25,26] which requires significant effort to position the target molecules within the "hotspot" such as incubation in solution[11−13] and integration with microfluidic systems.[5] As the enhanced EM wave decays exponentially from the surface to the surrounding media,[25,26] the effective plasmonic sensing areas of metallic structures are restricted within a few nanometers of the surfaces. Thus, a significant dimension mismatch exists between the nanoscale hotspot sensing area and the micro- or even macroscale distance of the species from the hotspot, resulting in extremely low efficiency for molecule immobilization or binding. For example, the solution incubation requires 12−24 h to attach the target molecules near the plasmonic hotspots for sensing.[11−13] Therefore, it is necessary to create an efficient interaction mechanism between the targeted species and the plasmonic hotspots through optimization of the binding process and the higher spatial overlap of the hotspot regions.

Optofluidic devices stand out as a promising candidate, which enables direct integration of plasmonic structure on a tubular microfluidic channel via a strain-induced self-rolling process.[27−30] Various plasmonic structures, including metallic bilayer,[27] patterned metasurface,[28,29] and graphene,[30] have been integrated in the microtubes, which spark novel plasmonic behavior and contribute to better sensitivity. Moreover, it demonstrates the possibility to lithographically

Received: June 20, 2020
Revised: August 17, 2020
Published: August 18, 2020

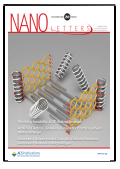

https://dx.doi.org/10.1021/acs.nanolett.0c02575
Nano Lett. 2020, 20, 6697−6705

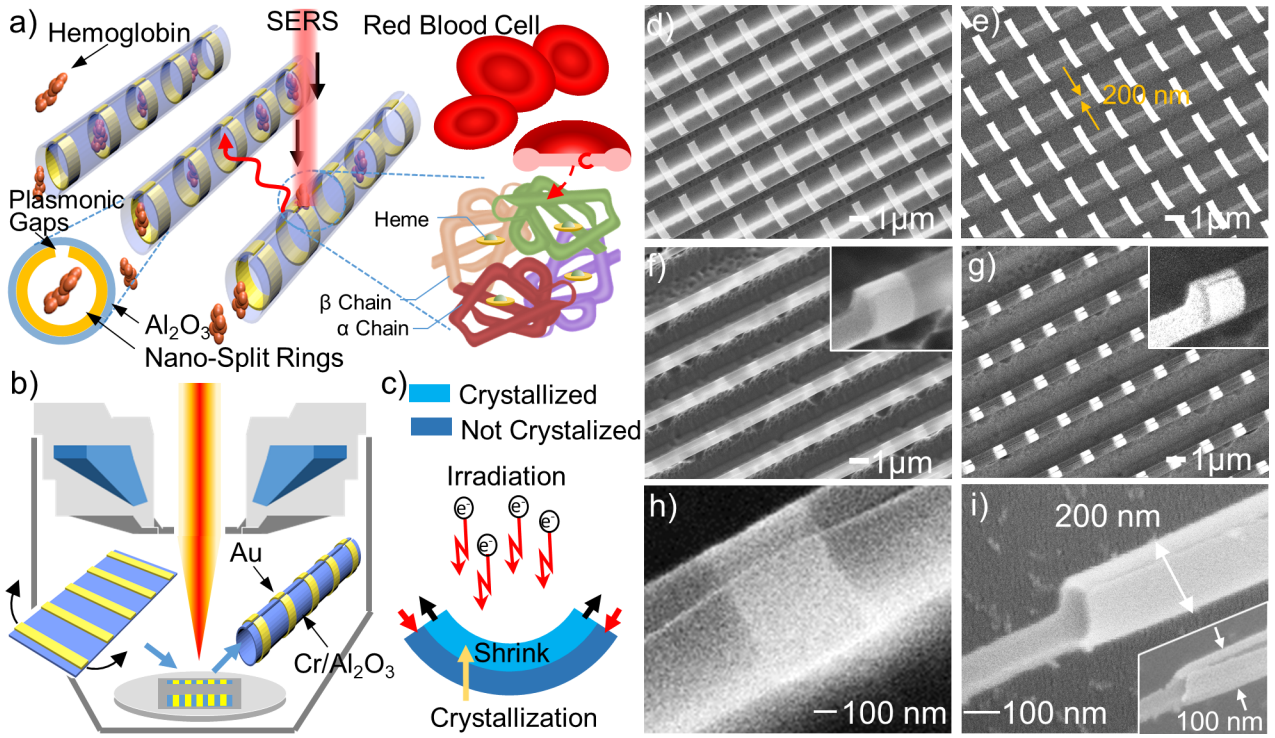

Figure 1. Conceptual schematics and SEM images showing the self-folding of nanocylinders with plasmonic nanogaps for bimolecular sensing. (a) Schematics showing the capability of using plasmonic nanocylinders for detecting hemoglobin. The nanosplit rings with gaps are formed on the inner surface of the nanocylinders and are directly exposed to the target molecule. (b) System setup and (c) mechanism of electron irradiation induced self-assembly. (d) SEM and (e) BSE images of the two-dimensional pattern (2 μm × 30 μm Cr/Al_2O_3 ribbon and 2 μm × 0.5 μm Cr/Au ribbon) before folding. The 2D patterns are partially released from the Si substrate while a 200 nm width contact area remained working as a supporting structure. (f) SEM and (g) BSE images of the self-assembled 3D nanocylinders with a diameter of ~640 nm. A nanogap is formed at the touching edges in the center of the nanocylinder. (h) The size of nanogaps achieved in the nanocylinder can reach sub-10 nm. (i) The nanocylinder can also be scaled down to 200 or 100 nm.

pattern plasmonic structures on the surface of microfluidic channels. However, as these devices are based on microscale tubes, the effective sensing regime is still confined to the surface, leaving plenty of target molecules in the center of flow undetectable. Furthermore, the plasmonic nanostructures defined on these microtubes are on the outer surface[28,30] or sandwiched with insulator layers[29] and not directly exposed to fluid (target molecule), which could further reduce sensitivity. Therefore, nanoscale optofluidic devices with plasmonic structures defined on the inner surface of nanocylinders are preferred to overcome the current limitations. Compared to the microfluidic channels, the spatial overlap of the plasmonic hotspot and the fluid flow is significantly improved in the nanofluidic channel, which increases the possibility to place the target molecule near and/or on the effective sensing regime and further improve the sensitivity.

Here, we present a hybrid system that achieves electromagnetic field enhancement and fluid confinement simultaneously by realizing 3D metallic surface patterns (nanosplit rings, NSRs) on the inner surface of cylindrical walls of curved nanofluidic channels (Figure 1). The patterns (3D NSRs) designed with gold (Au) form plasmonic gaps, serving as a plasmonic "hotspot" for molecular sensing. In addition, the 3D configuration of the nanocylinders enables fluid confinement with nanoscale dimensions which makes it possible to position chemical and biological substances close to the effective sensing regions in plasmonic structures defined on the inner surface of nanocylinders (Figure 1a). By bridging the gap between nanoplasmonics and nanofluidics, a more efficient interaction between the confined EM field and target molecule is achieved, contributing to higher sensitivity. Raman mapping of hemoglobin spectral fingerprints confirms the 3D metallic patterns on the curved nanofluidic channels as the dominant hotspot for sensing, providing a 22 times higher sensitivity compared to 2D structures.

The hybrid 3D plasmonic sensor (nanocylinders with NSRs) was fabricated through an electron irradiation induced self-assembly process (Figure 1b,c).[31] The 2D pattern before assembly consists of two components: an actuation bilayer of 1 nm thick chromium (Cr) and 5 nm thick aluminum oxide (Al_2O_3) and a metallic pattern of 5 nm gold (Au) (Figure 1d,e). After being released from silicon (Si) substrate, the 2D patterns are irradiated by electron streams. The electron irradiation (5 kV) enables the transformation of amorphous Al_2O_3 into crystal Al_2O_3, which is associated with significant volume reduction.[31] The volume change induces tensile and compression stress in the Al_2O_3/Cr layers, allowing the bilayer to curve up (Figure 1c). Once the two edges of the actuating bilayer touch, the curving process self-stops and forms nanocylinders (Figure 1f–i). The Au nanoribbons defined on the Al_2O_3 layer also curve up together with the actuation bilayer, which forms 3D NSRs. In addition, the self-stopping property allows the formation of a nanoscale plasmonic gap (sub-20 nm) at the edge of the Au ribbon (Figure 1f,h). A clear nanogap is observed in the self-assembled nanocylinder when analyzing their backscattered electron (BSE) image (Figure 1g) and zoomed in image (Figure 1h). As the formation of the nanogap is self-stopped, the size of the nanogap is uniform and

https://dx.doi.org/10.1021/acs.nanolett.0c02575
Nano Lett. 2020, 20, 6697−6705

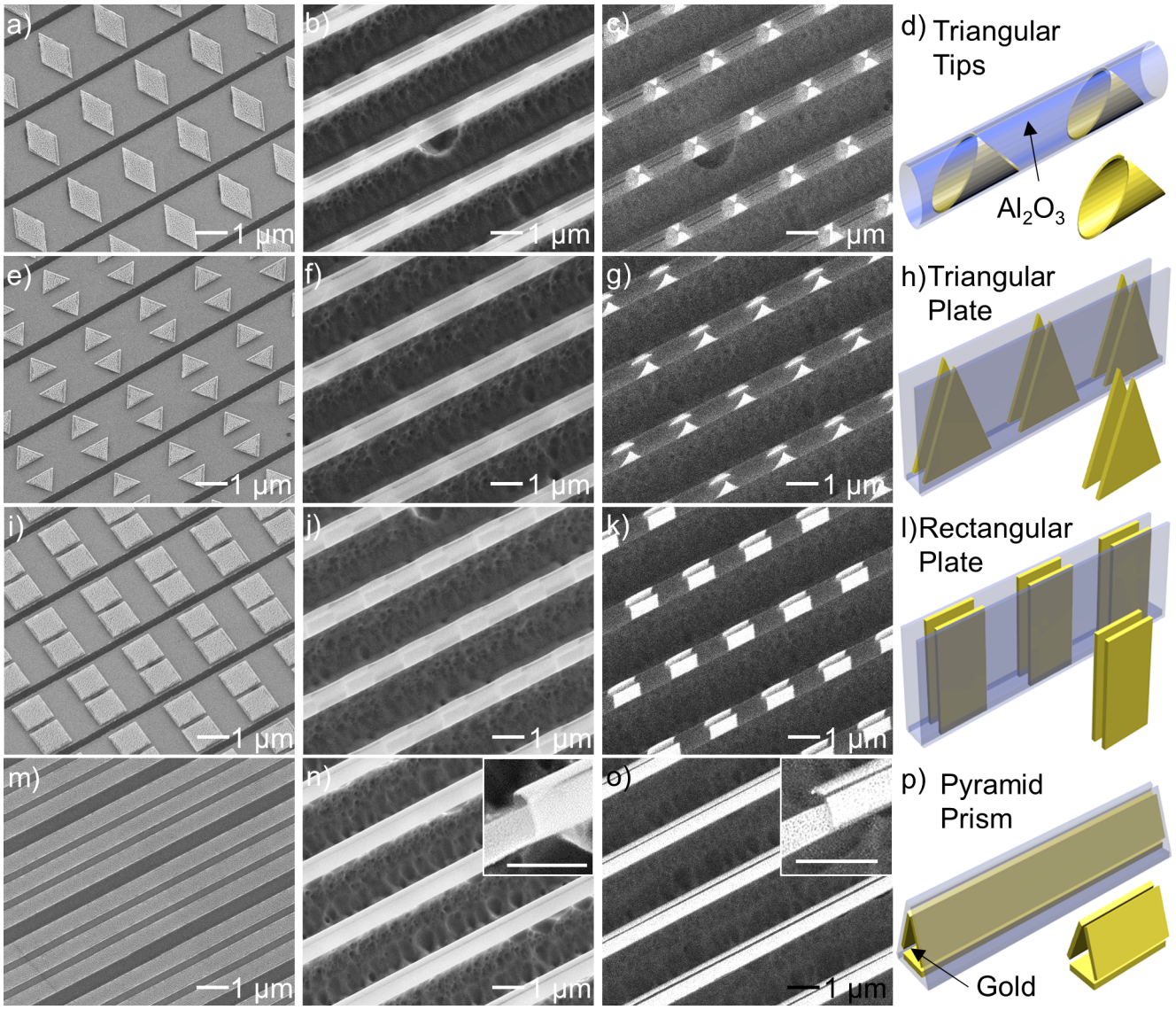

Figure 2. SEM, BSE, and conceptual schematics of different types of 3D plasmonic structures defined on the inner surface of nanotubes (nanocylinders, parallel plates, and prisms). The 2D designs of Au patterns determine the structure of both the plasmonic components and Al_2O_3 supporting components. (a–d) Triangular gold tips formed in nanocylinders, (e–h) triangular parallel plates, (i–l) rectangular parallel plates, and (m–p) pyramid prisms are demonstrated.

easily controlled (Figure S1) using an in situ monitored self-assembly process.[31] It should be noted that the size of the cylinder can be easily tuned to adjust the resonant frequency of NSRs by changing the dimension of the 2D patterns. Nanocylinder with smaller diameters of 200 and 100 nm have been realized to demonstrate the feasibility of scaling (Figure 1i). The detailed fabrication process is described in the Supporting Information Figure S2. A real-time monitored self-folding video is also provided in Supporting Information Video 1.

The nanocylinder with plasmonic nanogap achieves higher electric field enhancement through multiple benefits stemming from their geometrical form, namely, their curvature and the 3D nature of the gap. Simulation results from Comsol Multiphysics v5.4 for the plasmonic resonance in these nanocylinders compared to 2D plasmonics (Figure S3a-c) clearly show the higher intensity field enhancement close to the gap formed on the NSR. The 2D ribbon structure has no gap plasmons induced, showing minimal confinement at its edges; thus, the 3D gap plasmons in the nanocylinders (NSRs, Figure S3a) induce a field that is 40 times stronger than the field in the 2D ribbons (Figure S3b). Furthermore, even when comparing to 2D gap plasmons confined to a planar substrate, the 3D plasmons formed on the NSR continue to show nearly 20 times higher total field enhancement due to the curvature of the cylindrical gold layers causing lower losses from additional layers such as the underlying substrate or other dielectric layers (Figure S3c). Finally, even compared to 2D plasmonic gaps in suspended structures, the 3D cylindrical gap plasmons induce a total field enhancement that is 14 times stronger due to infinitesimal lateral lengths (cross-sectional area) approaching zero caused by the curvature that leads to small relaxation length available for gap plasmon (Figure S3d).

Furthermore, even among all the different types of 3D nanostructures, hollow nanocylinders offer the highest prospects due to the unique properties imparted by their morphology such as the large surface area to volume ratio. When cells are encapsulated in cylinder-based lab-on-chip

https://dx.doi.org/10.1021/acs.nanolett.0c02575
Nano Lett. 2020, 20, 6697–6705

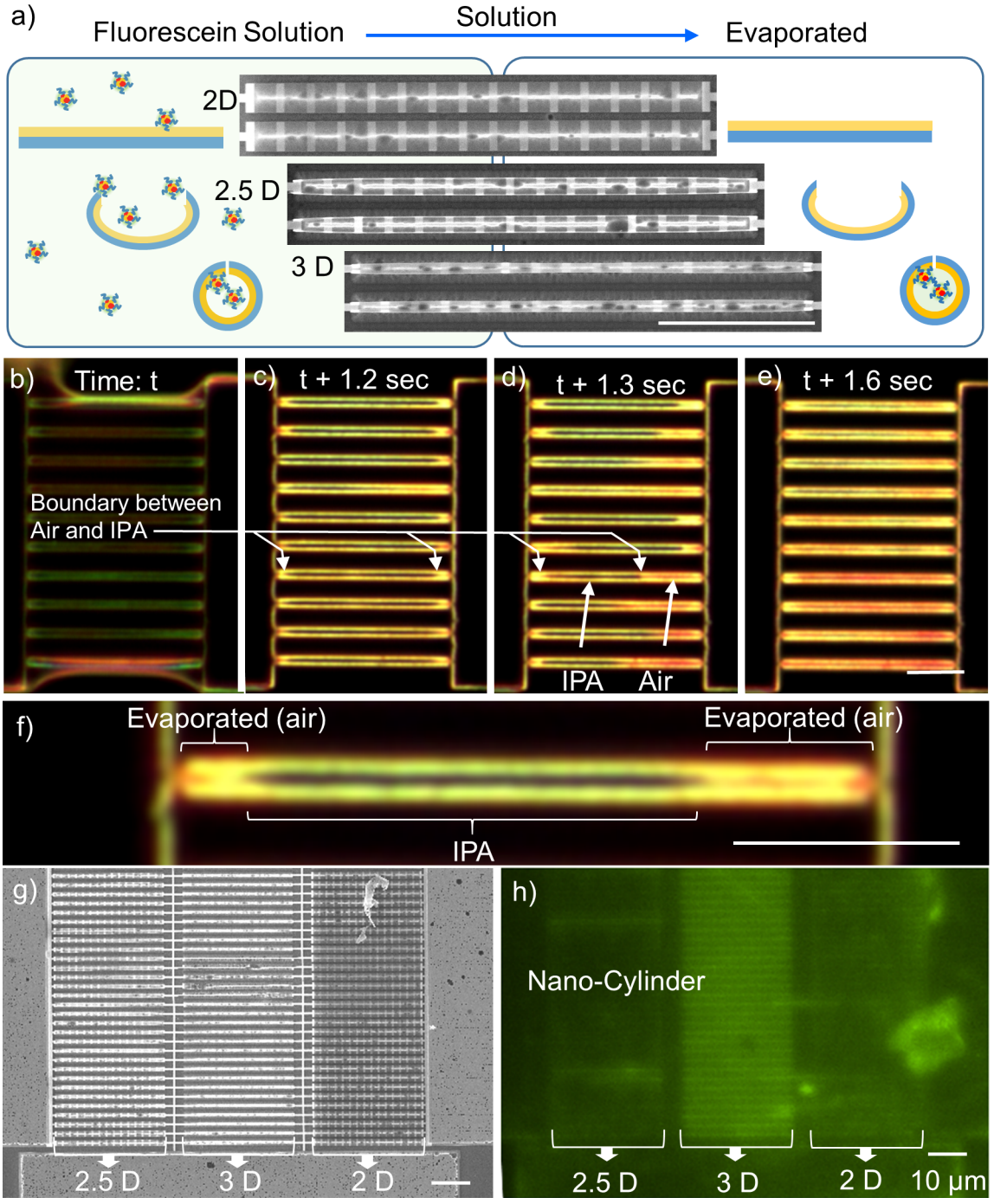

Figure 3. Characterization of fluid confinement on 2D ribbons, 2.5D halfway folded nanocylinders, and 3D nanocylinders using a fluorescent microscope. (a) Schematic showing the sample preparation for fluorescent measurement. (b−e) A dark-field optical microscope image confirming that fluid can flow in and out of the nanocylinder. (c−e) The movement of the fluid can be clearly observed inside the nanocylinder during the drying process. (f) A zoom-in image of the nanocylinder with 50% of IPA evaporated. (g) An SEM image of the samples before measurement. (h) A florescent image of the sample after treatment, showing enhanced fluid confinement in 3D nanocylinders.

devices, biological functions such as mitosis are preserved, thereby making nanocylinder-based sensors especially attractive.[32] The unique properties of nanocylinders, along with the ease of integration with microfluidic channels, have prompted research into their application for biological and chemical sensors and single cell analysis.[33−36] Thus, combining the superior gap plasmonics in the split-gap nanocylinders alongside ease of fluid confinement and target placement within a "hotspot" could yield rapid, accurate, and ultrahigh sensitivity technology for molecular analysis such as Raman analysis of hemoglobin (Hb) protein molecules (Figure 1a).

As already evident from the above discussion, the gap and layer morphology play a crucial role in determining the plasmonic modes that can be induced within them.[22] While diversity within 2D plasmonic structures[5,8,12] and 2D plasmon modes is severely limited by their basic geometrical forms and bounded gap plasmonic,[37] the self-assembly process is based on the deformation of 2D thin films, making it compatible with

https://dx.doi.org/10.1021/acs.nanolett.0c02575
Nano Lett. 2020, 20, 6697−6705

standard lithography processes for ease of incorporating a wide variety of 3D plasmonic architectures. The 2D patterns are transferred to 3D formats after self-assembly, resulting in diverse 3D plasmonic structures via tuning of the 2D gold patterns (Figure 2). The functional components of the 3D cylindrical plasmonic sensor are based on the plasmonic gaps formed between the touching edges of the Au ribbon. By changing the Au ribbon into a rhombus (Figure 2a), the short edges evolve into points, achieving plasmonic nanotips inside a nanocylinder after self-assembly (Figure 2b−d). Both the Au ribbons and rhombuses are continuous layers along the curving direction, which induces an equivalent deformation resistance from these layers during their self-assembly. Therefore, the deformation of the 2D pattern occurs in a curving format, creating nanocylinders (Figure 2a−d). Further, the curving behavior can be transformed into a folding process by adding a gap into the Au pattern (Figure 2e−p). During self-assembly, the Au patterns work as rigid materials and induce additional resistance for curing. The additional gaps in the Au pattern break the relative force equivalence along the curving direction (Figure 2e−i) and the gaps are more preferable locations for deformation, curving up prior to the rest of the structures. As a result, the curving process is transformed into a folding process that can realize triangular and rectangular parallel plate plasmonic structures (Figure 2f−h,j−l). Moreover, the parallel plate structure can evolve into a prism such as 3D triangular prisms by creating more gaps in the 2D Au patterns (Figure 2m−p). Among all of the fabricated 3D plasmonic structures, the gap plasmons in cylinders demonstrate the highest field intensity, which is 17 times higher field intensity than in the folded 3D structures (due to nonuniform gap spacing) (Figure S3a,e). In addition, the cylinders retain benefits of the 3D plasmons through location of hotspot, lower substrate losses, and fluid/particle confinement. Therefore, the cylinders are selected for the fluidic confinement and sensing measurement in this work. However, modification of the Au patterns and the gap between them opens the possibility to achieve more complex hollow, self-assembled geometries with a much higher tunability of the electromagnetic response from 3D plasmon modes.

The fluid flow and particle confinement in the hollow cylindrical nanostructures were experimentally investigated under dark-field and fluorescent microscopes. A sample that consists of 2D patterns, halfway curved nanocylinders (2.5D), and fully curved nanocylinders was prepared by the aforementioned fabrication process (Figure 3a). The 2D pattern has a width of 2 μm, which is assembled into a nanocylinder with a diameter of around 640 nm. Dark-field imaging, which enables the visualization of fluid flow via a color change, was carried out first to verify whether the liquid can fill the nanocylinder (Figure 3b−e). A drop of isopropyl alcohol (IPA) is placed on top of the fully curved nanocylinder arrays (Figure 3b). Because of evaporation, the volume of the IPA drop reduces, making it flow away from the nanocylinders (Figure 3c), and then the IPA inside the nanocylinder begins to evaporate. A clear boundary change from the fluid during evaporation is monitored under the dark-field microscope (Figure 3c−e), confirming that the fluid can be filled and confined inside the cylindrical volume despite finally evaporating through both ends of the cylinder (Figure 3e) after 2 s. Clearer evidence is shown in the zoomed-in dark-field image (Figure 3f). The 5 nm thick Al_2O_3 thin film enables the visualization of IPA inside the nanocylinder. The part of the nanocylinder filled with IPA shows a dark color while the empty nanocylinder shows a bright color. Also, a video shown the in situ observation of fluid confinement in nanocylinders is provided in Supporting Information Video 2. Further, a fluorescent measurement was conducted to evaluate the particle confinement behavior of the nanocylinder. The sample was dipped into a 2.5 mg/mL fluorescein-conjugated ovalbumin for 1 h and then rinsed thoroughly with water. Ovalbumin is a widely used protein molecule that consists of 385 amino acids, relative molecular mass of 42.7 kDa, and a minimum radius of ∼2 nm.[38] This value is similar to the common protein molecules, making ovalbumin a good representative example for a molecule confinement test.[39] In addition, the size of the florescent dye-conjugated ovalbumin, ∼2 nm, is much smaller than the diameter of the nanocylinder, ∼640 nm, allowing it flow into the chamber. Next, a 5 min water dip and gentle air gun dry out were utilized to clean up the molecules attached on samples and substrate. The florescent measurement was carried out on the washed sample using a fluorescence microscope. The detailed measurement setup and process are described in the Supporting Information. The measurement result shows a clear difference between the area of nanocylinders and the area of 2D ribbon and 2.5D halfway curved nanocylinders (Figure 3g,h). Much brighter fluorescence is observed on the fully curved nanocylinders, indicating that a fair number of molecules (the florescent dye) are still within the nanocylinder (Figure 3h). This observation demonstrates that the nanoscale cylindrical structure with a plasmonic gap not only allows the molecules to flow into it but also confines the molecules inside it with a higher efficiency. Compared to 2D patterns, the better molecular confinement in the nanocylinder makes it a passive trap to position the targeted molecules close to the hotspots, contributing to higher plasmonic sensitivity. By further scaling down the diameters of the nanocylinders, the average distances between the plasmonic hotspots and target molecules could be reduced. Thus, more molecules can be placed within the active sensing area of the plasmonic structures leading to a higher sensitivity in smaller cylindrical sensors. Nanocylinders with diameters of 200 and 100 nm are demonstrated (Figure 1i), which show the potential of this technique in pushing the limit of scaling.

Because of the superior gap plasmonics in the cylindrical split-ring (NSR) structures over other 3D forms, sensing capabilities of the nanocylinders were characterized based on SERS for an Hb molecule. Small size (∼5 nm in diameter)[41] and the well-established Hb fingerprints that range from 1000 to 1700 cm^{-1}[40] make it a suitable choice to flow through the nanocylinders. Also, a previous study demonstrates the capability to fill the hemoglobin molecule into a nanotube with a diameter of 250 nm by simply incubating the nanotubes in hemoglobin solution, which further shows that the number of the confined molecules can increase with higher concentration.[42] As the size of our cylinder is twice as large as the tube used in the previous work, the hemoglobin molecule should be able to flow into the nanocylinder successfully. Moreover, Hb is the oxygen-carrying protein inside red blood cells (RBCs), and abnormal Hb proteins are associated with various debilitating genetically inherited diseases.[43] For example, a single point mutation in the beta globin chain of Hb leads to the formation of rigid sickle-shaped RBCs in sickle cell disease (SCD) instead of discoid and flexible normal RBCs. SCD is the most common genetically inherited disease characterized by cumulative organ damage,

https://dx.doi.org/10.1021/acs.nanolett.0c02575
Nano Lett. 2020, 20, 6697−6705

pain, and reduced survival, which affects millions of individuals globally.[44,45] Mortality in SCD is high among all ages particularly among infants, which can be prevented with early screening for altered hemoglobin. Therefore, versatile and reproducible technologies like ours described herein can have an important application in SCD and other hemoglobinopathies.

For a quantitative comparison, 2D ribbons with width of 2 μm and the self-assembled nanocylinders with diameter of around 640 nm are defined on the Si substrate. The size of the NSR is carefully designed so that its resonant frequencies locate at 1354 and 1654 cm^{-1} (Figure S4), which are in the range of hemoglobin fingerprint peaks (1100−1700 cm^{-1}). In addition, the 2D ribbons and 3D nanocylinders were defined side by side on the same Si chip with a separation distance of 5 μm, which avoids different sample conditions except for dimensions (2D vs 3D) while the sample is prepared and characterized. To do the measurement, both 2D ribbon and 3D (configured with split rings) samples were dipped into a 2.5 mg/mL Hb solution for 5 min and later dried out by air gun. The detailed system setup and process for SERS measurement are provided in Supporting Information. The collected Raman spectra show prominent Hb fingerprints with amino acid valine peak at 1127 cm^{-1} and phenylalanine peak at 1583 cm^{-1}[46] (the peak at ∼1000 cm^{-1} is attributed to the Si substrate). The signal detected from 2D regions of the sample transduces an extremely low intensity (Figure 4a) causing it to be easily masked by noise from impurities or surface imperfections, substrate losses, and diffusion limitations at low concentrations of the molecules for analysis. However, these two modes are significantly enhanced by the 3D plasmonic structures configured with NSRs (Figure 4a). An enhancement factor (EF) of ∼10 is observed based on the ratio of Raman peak intensity at the plasmonic gaps of 3D nanosplit rings (I_{3D}) over the peak intensity at 2D Au ribbons (I_{2D}). The enhancement is attributed to three factors: (1) The superior light confinement by 3D gap plasmon induced in NSRs, (2) the ability of the cylindrical structure to perform fluid confinement, and (3) lower losses to the underlying substrate from the suspended architecture.

The contribution of each of these three factors can be individually characterized by a spatial imaging of SERS, where the laser was scanned over both the 2D and 3D sample areas and Raman spectra were collected as a function of positions, which generate Raman maps (Figure 4b,d). The Raman maps corresponding to the peak intensities of 1583 cm^{-1} were collected at each pixel of the 2D ribbon (Figure 4c) and 3D NSRs on nanocylinders (Figure 4e). Clearly, the Raman peak intensities from the plasmonic gaps in cylindrical structure are much higher than that of 2D ribbons throughout the measurement area (Figure 4b,d), which shows the advantage of using plasmonic nanocylinders as molecular sensors. The variation in intensity across a given section shows that the plasmonic gap in the presence of Hb molecules induces a maximum intensity of 212 CCD counts (Figure 4f). Because of variations in the number of molecules at the plasmonic gap for a lower concentration of Hb molecules, a CCD count of 134 is still achieved as the lowest intensity from nanocylinders (Figure 4f). In comparison, the cylinders without gold plasmonic structures (NSRs) with only fluid confinement can still achieve an average intensity of ∼34.5 CCD counts while the 2D gold ribbon structure can only achieve an average intensity of 9.4 CCD counts (Figure 4f). This implies that the fluid confinement enhances the Raman signal by 3.7 times, which is attributed to liquid confinement of the nanocylinder as well as the hemoglobin trapped inside the nanocylinder.

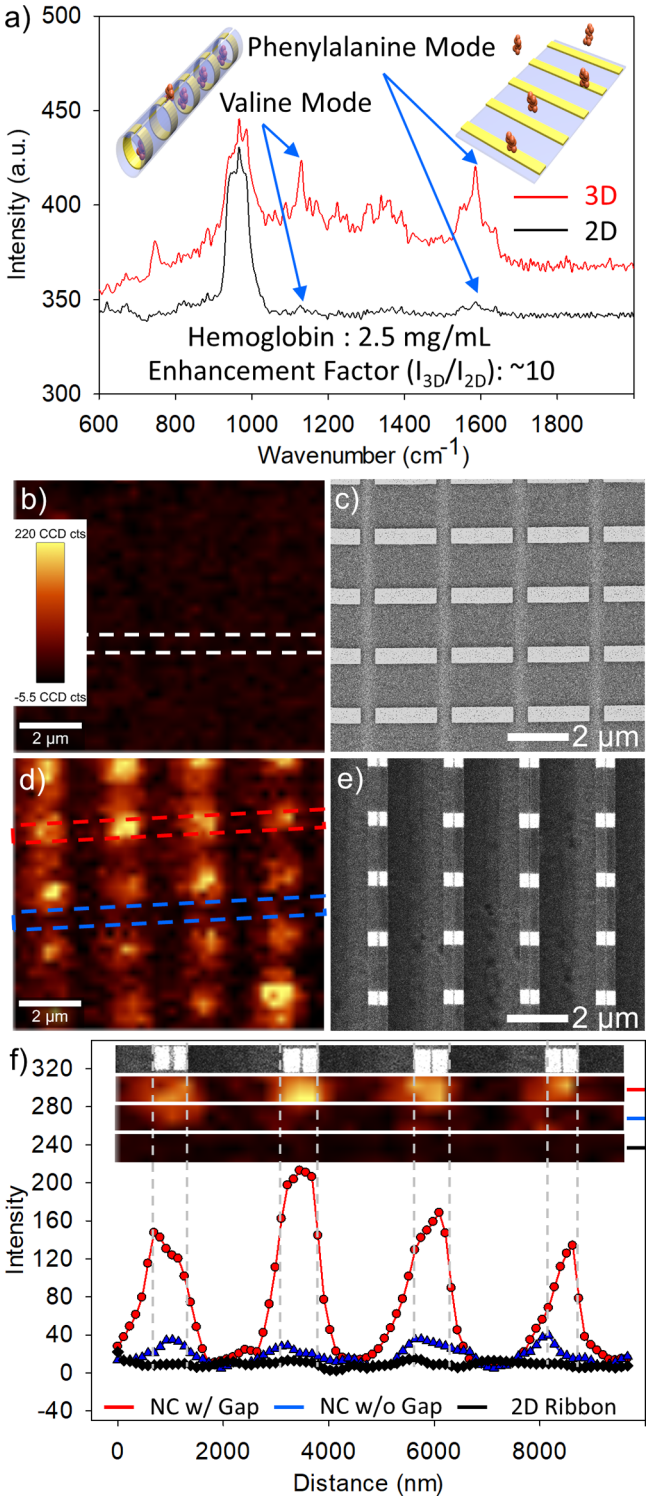

Figure 4. Raman analysis of hemoglobin. (a) Raman spectra of hemoglobin from 2D ribbons before folding and 3D nanocylinder (NC) with plasmonic gaps. (b) Raman imaging collected on (c) 2D ribbon sample based on the peak at 1600 cm^{-1}. (d) Raman imaging collected on (e) 3D nanocylinder sample based on the peak at 1600 cm^{-1}. Strong hotspots are observed around the plasmonic nanogap. (f) Raman intensity across the area highlighted in (b,d). Much higher intensity is achieved on the gold rings with plasmonic gaps.

https://dx.doi.org/10.1021/acs.nanolett.0c02575
Nano Lett. 2020, 20, 6697−6705

Furthermore, the interactions with the 40 times higher enhanced field by the 3D gap plasmons in NSRs result in a total Raman intensity enhancement of ∼22 times. This coherence of the Raman mapping confirms that the 3D gap plasmons are uniform and reliable hotspots acting as the main contributors for the higher sensitivity. This result demonstrates that the advanced sensing capability is attributed to the three-fold advantages of plasmonic nanocylinders: (i) the superior light confinement induced by 3D gap plasmon of NSRs, (ii) the ability to achieve fluid confinement in the nanoscale cylindrical structures, and (iii) lower energy losses to the underlying substrate from the suspended architecture. These effects collectively leave a spectral fingerprint (Figure 4a) with an ∼10 times higher peak intensity compared to 2D ribbons. The enhancement of this optofluidic sensing technique for detecting hemoglobin is more significant than graphene-enhanced Raman scattering[40] but not as comparable to nanoparticle-based Raman techniques.[47] The uniformity of Raman signal is evaluated based on the signal collected at each NSR area (500 nm × 500 nm) on the Raman map. As shown in Figure S5, more than 50% of the collected signals have the intensity between 80 to 120, which presents the level of uniformity. Variations exist due to nonuniform hemoglobin distribution and nanogap sizes. Though there are still some limitations, this technique offers a new strategy to form a plasmonic hotspot using self-assembly and simultaneously allows integration with nanofluidic systems. Its sensitivity could be further enhanced by optimization of the plasmonic pattern design, structure dimension, and uniformity.

In conclusion, nanoplasmonics can be bridged with nanofluidics using an e-beam triggered self-assembly. Through self-assembly, the 2D ribbons with surface patterned Au structures are curved into cylindrical nanochannels to induce 3D plasmon modes with orders of magnitude superior field confinement. The integration of a plasmonic nanostructure into a nanoscale channel makes it possible to achieve field enhancement and fluid confinement simultaneously, resulting in 22 times higher sensitivity. This hybrid system might open the possibility to explore interactions between 3D plasmonic structures and nanoscale volume of targeted species for highly efficient sensing techniques.

■ ASSOCIATED CONTENT

Supporting Information

The Supporting Information is available free of charge at https://pubs.acs.org/doi/10.1021/acs.nanolett.0c02575.

Gap size distribution, fabrication process of plasmonic nanocylinders, Comsol Multiphysics simulation of plasmonic behaviors, fluorescence measurement, resonance of nanosplit ring, SERS measurement, and Raman hotspot distribution (PDF)

Video 1: Real-time video of self-assembly process (MP4)

Video 2: In situ observation of fluid flow and subsequent confinement in the plasmonic nanocylinders (MP4)

■ AUTHOR INFORMATION

Corresponding Author

Jeong-Hyun Cho − *Department of Electrical and Computer Engineering, University of Minnesota, Minneapolis, Minnesota 55455, United States;* orcid.org/0000-0003-2870-1960; Email: jcho@umn.edu

Authors

Chunhui Dai − *Department of Electrical and Computer Engineering, University of Minnesota, Minneapolis, Minnesota 55455, United States*

Zihao Lin − *Department of Electrical and Computer Engineering, University of Minnesota, Minneapolis, Minnesota 55455, United States*

Kriti Agarwal − *Department of Electrical and Computer Engineering, University of Minnesota, Minneapolis, Minnesota 55455, United States*

Carol Mikhael − *Department of Electrical and Computer Engineering, University of Minnesota, Minneapolis, Minnesota 55455, United States*

Anupam Aich − *Hematology/Oncology Division, Department of Medicine, University of California, Irvine, California 92697, United States*

Kalpna Gupta − *Hematology/Oncology Division, Department of Medicine, University of California, Irvine, California 92697, United States; Division of Hematology, Oncology and Transplantation, University of Minnesota, Minneapolis, Minnesota 55455, United States; SCIRE, Veterans Affairs Medical Center, Long Beach, California 90822, United States*

Complete contact information is available at: https://pubs.acs.org/10.1021/acs.nanolett.0c02575

Notes

The authors declare no competing financial interest.

■ ACKNOWLEDGMENTS

This research was supported by the National Science Foundation under Grant CMMI-1454293. Portions of this work were conducted in the Minnesota Nano Center, which is supported by the National Science Foundation through the National Nano Coordinated Infrastructure Network (NNCI) under Award Number ECCS-1542202. Parts of this work were carried out in the Characterization Facility, University of Minnesota, a member of the NSF-funded Materials Research Facilities Network (www.mrfn.org) via the MRSEC program. This work was supported partially by the National Science Foundation through the University of Minnesota MRSEC under Award Number DMR-2011401 and a grant from University of Minnesota Informatics Institute, which includes support from the University of Minnesota's MnDRIVE Initiative. The authors acknowledge the Minnesota Supercomputing Institute (MSI) at the University of Minnesota for providing resources that contributed to the research results reported within this paper. C.D. acknowledges the support from Doctoral Dissertation Fellowship from University of Minnesota. K.G. acknowledges support from NIH RO1 HL147562. KG disclosures Honoraria: Tautona Group, Novartis and CSL Behring. Research Grants: Cyclerion, 1910 Genetics and Grifols. All others: Nothing to disclose. *The content is solely the responsibility of the authors and does not necessarily represent the official views of the National Institutes of Health.*

■ REFERENCES

(1) Lal, S.; Link, S.; Halas, N. J. Nano-optics from sensing to waveguiding. *Nat. Photonics* **2007**, *1*, 641.

(2) Nagpal, P.; Lindquist, N. C.; Oh, S. H.; Norris, D. J. Ultrasmooth patterned metals for plasmonics and metamaterials. *Science* **2009**, *325*, 594−597.

(3) Jung, K.; Hahn, J.; In, S.; Bae, Y.; Lee, H.; Pikhitsa, P. V.; Ahn, K.; Ha, K.; Lee, J.-K.; Park, N.; Choi, M. Hotspot-engineered 3D multipetal flower assemblies for surface-enhanced Raman spectroscopy. *Adv. Mater.* **2014**, *26*, 5924−5929.
(4) De Angelis, F.; Malerba, M.; Patrini, M.; Miele, E.; Das, G.; Toma, A.; Zaccaria, R. P.; Di Fabrizio, E. 3D hollow nanostructures as building blocks for multifunctional plasmonics. *Nano Lett.* **2013**, *13*, 3553−3558.
(5) Vázquez-Guardado, A.; Barkam, S.; Peppler, M.; Biswas, A.; Dennis, W.; Das, S.; Seal, S.; Chanda, D. Enzyme-free plasmonic biosensor for direct detection of neurotransmitter dopamine from whole blood. *Nano Lett.* **2019**, *19*, 449−454.
(6) Lin, E.; Fang, J.; Park, S.; Johnson, F. W.; Jacobs, H. O. Effective localized collection and identification of airborne species through electrodynamic precipitation and SERS-based detection. *Nat. Commun.* **2013**, *4*, 1−8.
(7) Dipalo, M.; Messina, G. C.; Amin, H.; La Rocca, R.; Shalabaeva, V.; Simi, A.; Maccione, A.; Zilio, P.; Berdondini, L.; De Angelis, F. 3D plasmonic nanoantennas integrated with MEA biosensors. *Nanoscale* **2015**, *7*, 3703−3711.
(8) Tinguely, J.; Sow, I.; Leiner, C.; Grand, J.; Hohenau, A.; Felidj, N.; Aubard, J.; Krenn, J. R. Gold nanoparticles for plasmonic biosensing: the role of metal crystallinity and nanoscale roughness. *Bionanoscience* **2011**, *1*, 128−135.
(9) Leem, J.; Wang, M. C.; Kang, P.; Nam, S. Mechanically self-assembled, three-dimensional graphene−gold hybrid nanostructures for advanced nanoplasmonic sensors. *Nano Lett.* **2015**, *15*, 7684−7690.
(10) Huck, C.; Neubrech, F.; Vogt, J.; Toma, A.; Gerbert, D.; Katzmann, J.; Hartling, T.; Pucci, A. Surface-enhanced infrared spectroscopy using nanometer-sized gaps. *ACS Nano* **2014**, *8*, 4908−4914.
(11) Chen, C.; Mohr, D. A.; Choi, H.; Yoo, D.; Li, M.; Oh, S. Waveguide-integrated compact plasmonic resonators for on-chip mid-infrared laser spectroscopy. *Nano Lett.* **2018**, *18*, 7601−7608.
(12) Im, H.; Bantz, K. C.; Lindquist, N. C.; Haynes, C. L.; Oh, S. Vertically oriented sub-10-nm plasmonic nanogap arrays. *Nano Lett.* **2010**, *10*, 2231−2236.
(13) Im, H.; Bantz, K. C.; Lee, S. H.; Johnson, T. W.; Haynes, C. L.; Oh, S. Self-assembled plasmonic nanoring cavity arrays for SERS and LSPR biosensing. *Adv. Mater.* **2013**, *25*, 2678−2685.
(14) Miyazaki, C. M.; Shimizu, F. M.; Ferreira, M. Surface plasmon resonance (SPR) for sensors and biosensors. In *Nanocharacterization Techniques*; de Oliveira, O., Jr., Ferreira, L., Marystela, G., de Lima Leite, F., Da Róz, A. L., Eds.; Elsevier, 2017; pp 183−200.
(15) Chen, X.; Ciracì, C.; Smith, D. R.; Oh, S. Nanogap-enhanced infrared spectroscopy with template-stripped wafer-scale arrays of buried plasmonic cavities. *Nano Lett.* **2015**, *15*, 107−113.
(16) Malerba, M.; Alabastri, A.; Miele, E.; Zilio, P.; Patrini, M.; Bajoni, D.; Messina, G. C.; Dipalo, M.; Toma, A.; Proietti Zaccaria, R.; De Angelis, F. 3D vertical nanostructures for enhanced infrared plasmonics. *Sci. Rep.* **2015**, *5*, 16436.
(17) Jubb, A. M.; Jiao, Y.; Eres, G.; Retterer, S. T.; Gu, B. Elevated gold ellipse nanoantenna dimers as sensitive and tunable surface enhanced Raman spectroscopy substrates. *Nanoscale* **2016**, *8*, 5641−5648.
(18) Hatab, N. A.; Hsueh, C.; Gaddis, A. L.; Retterer, S. T.; Li, J.; Eres, G.; Zhang, Z.; Gu, B. Free-standing optical gold bowtie nanoantenna with variable gap size for enhanced Raman spectroscopy. *Nano Lett.* **2010**, *10*, 4952−4955.
(19) Lin, S.; Hatab, N. A.; Gu, B.; Chao, B.; Li, J.; Hsueh, C. Free-standing gold elliptical nanoantenna with tunable wavelength in near-infrared region for enhanced Raman spectroscopy. *Appl. Phys. A: Mater. Sci. Process.* **2016**, *122*, 674.
(20) Lin, E.; Fang, J.; Park, S.; Stauden, T.; Pezoldt, J.; Jacobs, H. O. Effective collection and detection of airborne species using SERS-based detection and localized electrodynamic precipitation. *Adv. Mater.* **2013**, *25*, 3554−3559.
(21) Fang, J.; Park, S.; Schlag, L.; Stauden, T.; Pezoldt, J.; Jacobs, H. O. Localized collection of airborne analytes: a transport driven approach to improve the response time of existing gas sensor designs. *Adv. Funct. Mater.* **2014**, *24*, 3706−3714.
(22) Yoo, D.; Johnson, T. W.; Cherukulappurath, S.; Norris, D. J.; Oh, S. Template-stripped tunable plasmonic devices on stretchable and rollable substrates. *ACS Nano* **2015**, *9*, 10647−10654.
(23) Hentschel, M.; Schäferling, M.; Duan, X.; Giessen, H.; Liu, N. Chiral plasmonics. *Sci. Adv.* **2017**, *3*, No. e1602735.
(24) Shen, X.; Song, C.; Wang, J.; Shi, D.; Wang, Z.; Liu, N.; Ding, B. Rolling up gold nanoparticle-dressed DNA origami into three-dimensional plasmonic chiral nanostructures. *J. Am. Chem. Soc.* **2012**, *134*, 146−149.
(25) Homola, J.; Yee, S. S.; Gauglitz, G. Surface plasmon resonance sensors. *Sens. Actuators, B* **1999**, *54*, 3−15.
(26) Barnes, W. L.; Dereux, A.; Ebbesen, T. W. Surface plasmon subwavelength optics. *Nature* **2003**, *424*, 824−830.
(27) Yin, Y.; Qiu, T.; Ma, L.; Lang, X.; Zhang, Y.; Huang, G.; Mei, Y.; Schmidt, O. G. Exploring rolled-up Au−Ag bimetallic microtubes for surface enhanced raman scattering sensor. *J. Phys. Chem. C* **2012**, *116*, 25504−25508.
(28) Yin, Y.; Li, S.; Böttner, S.; Yuan, F.; Giudicatti, S.; Saei Ghareh Naz, E.; Ma, L.; Schmidt, O. G. "Localized surface plasmons selectively coupled to resonant light in tubular microcavities.". *Phys. Rev. Lett.* **2016**, *116*, 253904.
(29) Bermúdez-Ureña, E.; Steiner, U. Self-rolled multilayer metasurfaces. *ACS Photonics* **2019**, *6*, 2198−2204.
(30) Yin, Y.; Pang, J.; Wang, J.; Lu, X.; Hao, Q.; Saei Ghareh Naz, E.; Zhou, X.; Ma, L.; Schmidt, O. G. Graphene-activated optoplasmonic nanomembrane cavities for photodegradation detection. *ACS Appl. Mater. Interfaces* **2019**, *11*, 15891−15897.
(31) Dai, C.; Li, L.; Wratkowski, D.; Cho, J. H. Electron Irradiation Driven Nanohands for Sequential Origami. *Nano Lett.* **2020**, *20*, 4975−4984.
(32) Xi, W.; Schmidt, C. K.; Sanchez, S.; Gracias, D. H.; Carazo-Salas, R. E.; Butler, R.; Lawrence, N.; Jackson, S. P.; Schmidt, O. G. Molecular insights into division of single human cancer cells in on-chip transparent microtubes. *ACS Nano* **2016**, *10*, 5835−5846.
(33) Madani, A.; Kleinert, M.; Stolarek, D.; Zimmermann, L.; Ma, L.; Schmidt, O. G. Vertical optical ring resonators fully integrated with nanophotonic waveguides on silicon-on-insulator substrates. *Opt. Lett.* **2015**, *40*, 3826−3829.
(34) Miao, S.; Chen, D.; Madani, A.; Jorgensen, M. R.; Bolaños Quiñones, V. A.; Ma, L.; Hickey, S. G.; Eychmüller, A.; Schmidt, O. G. Optofluidic Sensor: Evaporation Kinetics Detection of Solvents Dissolved with Cd3P2 Colloidal Quantum Dots in a Rolled-Up Microtube. *Adv. Opt. Mater.* **2015**, *3*, 187−193.
(35) Weiz, S. M.; Medina-Sánchez, M.; Schmidt, O. G. Microsystems for Single-Cell Analysis. *Adv. Biosyst.* **2018**, *2*, 1700193.
(36) Smith, E. J.; Schulze, S.; Kiravittaya, S.; Mei, Y.; Sanchez, S.; Schmidt, O. G. Lab-in-a-tube: detection of individual mouse cells for analysis in flexible split-wall microtube resonator sensors. *Nano Lett.* **2011**, *11*, 4037−4042.
(37) Agarwal, K.; Dai, C.; Joung, D.; Cho, J. Nano-Architecture Driven Plasmonic Field Enhancement in 3D Graphene Structures. *ACS Nano* **2019**, *13*, 1050−1059.
(38) Stein, P. E.; Leslie, A. G.; Finch, J. T.; Carrell, R. W. Crystal structure of uncleaved ovalbumin at 1· 95 Å resolution. *J. Mol. Biol.* **1991**, *221*, 941−959.
(39) Kozlowski, L. P. Proteome-pI: proteome isoelectric point database. *Nucleic Acids Res.* **2017**, *45*, D1112−D1116.
(40) Huang, S.; Pandey, R.; Barman, I.; Kong, J.; Dresselhaus, M. Raman enhancement of blood constituent proteins using graphene. *ACS Photonics* **2018**, *5*, 2978−2982.
(41) Erickson, H. P. Size and shape of protein molecules at the nanometer level determined by sedimentation, gel filtration, and electron microscopy. *Biol. Proced. Online* **2009**, *11*, 32.
(42) Mandal, S. S.; Nagarajan, B.; Amenitsch, H.; Bhattacharyya, A. J. Probing hemoglobin confinement inside submicron silica tubes

https://dx.doi.org/10.1021/acs.nanolett.0c02575
Nano Lett. 2020, 20, 6697−6705

using synchrotron SAXS and electrochemical response. *Eur. Biophys. J.* **2013**, *42*, 371−382.
(43) Cavazzana, M.; Antoniani, C.; Miccio, A. Gene therapy for β-hemoglobinopathies. *Mol. Ther.* **2017**, *25*, 1142−1154.
(44) Telen, M. J.; Malik, P.; Vercellotti, G. M. Therapeutic strategies for sickle cell disease: towards a multi-agent approach. *Nat. Rev. Drug Discovery* **2019**, *18*, 139−158.
(45) Kato, G. J.; Piel, F. B.; Reid, C. D.; Gaston, M. H.; Ohene-Frempong, K.; Krishnamurti, L.; Smith, W. R.; Panepinto, J. A.; Weatherall, D. J.; Costa, F. F.; Vichinsky, E. P. Sickle cell disease. *Nat. Rev.* **2018**, *4*, 1−22.
(46) Lin, J.; Lin, J.; Huang, Z.; Lu, P.; Wang, J.; Wang, X.; Chen, R. Raman spectroscopy of human hemoglobin of diabetes detection. *J. Innovative Opt. Health Sci.* **2014**, *07*, 1350051.
(47) Kang, Y.; Si, M.; Liu, R.; Qiao, S. Surface-enhanced Raman scattering (SERS) spectra of hemoglobin on nano silver film prepared by electrolysis method. *J. Raman Spectrosc.* **2010**, *41*, 614−617.

https://dx.doi.org/10.1021/acs.nanolett.0c02575
Nano Lett. 2020, 20, 6697−6705